Variations of characteristic time scales in rotating stratified turbulence using a large parametric numerical study

D. Rosenberg, R. Marino, C. Herbert, A. Pouquet

Variations of characteristic time scales in rotating stratified turbulence using a large parametric numerical study*

D. Rosenberg[1,2], R. Marino[3,4], C. Herbert[5], and A. Pouquet[6,7,a]

[1] National Center for Computational Sciences, Oak Ridge National Laboratory, P.O. Box 2008, Oak Ridge, TN 37831, USA
[2] SciTec, Inc., 100 Wall St. Princeton, NJ 08540, USA
[3] École Normale Supérieure, Lyon, F-69007, France
[4] Space Sciences Laboratory, University of California, Berkeley, CA 94720, USA
[5] Department of Physics of Complex Systems, Weizmann Institute of Science, 76100 Rehovot, Israel
[6] Laboratory for Atmospheric and Space Physics, University of Colorado, Boulder, CO 80309, USA
[7] National Center for Atmospheric Research, P.O. Box 3000, Boulder, CO 80307, USA

Received 7 October 2015 and Received in final form 16 December 2015
Published online: 29 January 2016 –

Abstract. We study rotating stratified turbulence (RST) making use of numerical data stemming from a large parametric study varying the Reynolds, Froude and Rossby numbers, Re, Fr and Ro in a broad range of values. The computations are performed using periodic boundary conditions on grids of 1024^3 points, with no modeling of the small scales, no forcing and with large-scale random initial conditions for the velocity field only, and there are altogether 65 runs analyzed in this paper. The buoyancy Reynolds number defined as $\mathcal{R}_B = ReFr^2$ varies from negligible values to $\approx 10^5$, approaching atmospheric or oceanic regimes. This preliminary analysis deals with the variation of characteristic time scales of RST with dimensionless parameters, focusing on the role played by the partition of energy between the kinetic and potential modes, as a key ingredient for modeling the dynamics of such flows. We find that neither rotation nor the ratio of the Brunt-Väisälä frequency to the inertial frequency seem to play a major role in the absence of forcing in the global dynamics of the small-scale kinetic and potential modes. Specifically, in these computations, mostly in regimes of wave turbulence, characteristic times based on the ratio of energy to dissipation of the velocity and temperature fluctuations, T_V and T_P, vary substantially with parameters. Their ratio $\gamma = T_V/T_P$ follows roughly a bell-shaped curve in terms of Richardson number Ri. It reaches a plateau —on which time scales become comparable, $\gamma \approx 0.6$— when the turbulence has significantly strengthened, leading to numerous destabilization events together with a tendency towards an isotropization of the flow.

1 Introduction

A salient property of turbulent flows is the high amount of dissipation that occurs in them through the formation of small-scale structures stemming from the nonlinear dynamics due to advection by the velocity field. Although not proven mathematically, it is conjectured that in the limit of infinite Reynolds number $Re = U_0 L_0/\nu$ (or zero kinematic viscosity ν), the dissipation of the flow tends to unity when properly adimensionalized. In other words, for a flow with characteristic velocity $U_0 = 1$ and length scale $L_0 = 1$, the dimensional evaluation of dissipation $\epsilon_D = U_0^3/L_0 \approx 1$ is realized by the flow through the formation of ever thinner vorticity sheets and filaments, similar to the case of coupling to a magnetic field in the magnetohydrodynamic (MHD) limit, which shows ever thinner current sheets. This means that strongly localized structures, both in space and time, are observed and these extreme events can be associated with anomalous wings in probability distribution functions of velocity gradients, when compared to the Gaussian law. Using high-resolution direct numerical simulations (DNS) of the relevant Navier-Stokes equations in the incompressible case, one can measure the dissipation rate $\epsilon = -\mathrm{d}E/\mathrm{d}t$, where E is the total energy. A tendency towards a constant dissipation rate of order unity is observed both for fluids [1] (see [2] for the supersonic case), and for MHD [3].

On the other hand, strong waves are observed in the atmosphere and the ocean due to rotation and stratification, and in the heliosphere and beyond because of the presence of a large-scale magnetic field (see *e.g.* [4,5]), and the amount of effective dissipation occurring at high

Reynolds number in the presence of waves is an open problem. For example, the transfer of energy from internal tides to the small-scale flow can be enhanced through bottom topography, as observed in the ocean [6], and as studied in the laboratory using particle image velocimetry [7]. In the linear limit when the advection term can be completely neglected, there is no nonlinear wave coupling and no dissipation will occur at high Re. Of course, weak coupling between waves does take place, *e.g.* through 3-wave resonances; this coupling leads to some energy being transferred to the small scales where it can be dissipated, but in what amount, and what are the relevant time scales for dissipation to occur? This limit of wave turbulence is valid when the characteristic period of a wave, T_W, is much shorter than the eddy turn-over time $\tau_{NL} = L_0/U_0$, as measured for example by the Froude and Rossby numbers, Fr and Ro (see sect. 2 for definitions). Weak turbulence has been studied at length, analytically, observationally, numerically as well as in the laboratory (see [8–12] for reviews and [13–15] for recent developments including for quantum turbulence [16]). Solutions can be found that describe the energy distribution among waves (see [17,18] for rotating and magnetohydrodynamics turbulence respectively, and [19] in the atmospheric context). However, such a limit is non-uniform since T_W and τ_{NL} have different variations with scale and hence strong, fast eddies are bound to be found at small scales for fluid turbulence. Phenomenology can help devise many scaling solutions (see *e.g.* [20–24]) and multiple data sets are needed to sort out the different regimes that can arise under such complex behavior governed by several dimensionless parameters.

It is in this context that we analyze the dissipative properties of a series of runs performed using direct numerical simulations on grids of $n_p^3 = 1024^3$ points for a large range of parameters chosen to fit either oceanic conditions (with low Froude number and low Ro/Fr) as well as atmospheric conditions, with higher Fr and higher Ro/Fr. On the other hand, Reynolds numbers in these DNS runs are at most 18×10^3, well below those encountered in geophysical fluid dynamics, a limitation due to the cost of performing DNS that we will experience for some time to come unless some form of modeling is used, as is customary in most atmospheric, oceanic and climatological studies.

2 Equations

Neglecting both moisture in the atmosphere and salinity in the ocean, the Boussinesq equations are a useful approach to study the dynamics of geophysical flows in the presence of rotation and stable stratification, both of which we take to be imposed in the z direction and constant in magnitude (see *e.g.* [25]). They read:

$$\partial_t \mathbf{u} - \nu \Delta \mathbf{u} + N\theta \hat{z} + \nabla p - f \mathbf{u} \times \hat{z} = -\mathbf{u} \cdot \nabla \mathbf{u}, \quad (1)$$

$$\partial_t \theta - \kappa \Delta \theta - N w = -\mathbf{u} \cdot \nabla \theta \,, \quad (2)$$

with $\mathbf{u} = (u, v, w)$ the velocity field which is taken to be incompressible, $\nabla \cdot \mathbf{u} = 0$; p is the pressure, and θ represents the temperature (or density) fluctuations, superimposed on a linear background profile $\bar{\theta}(z) = \theta_0 + z\partial_z \bar{\theta}$, with $\partial_z \bar{\theta} < 0$, with a constant mean temperature gradient $\partial_z \theta(z)$; note that the potential energy density is proportional to $\theta(\mathbf{x})^2$ since in the above formulation of the Boussinesq equations, temperature fluctuations have the dimension of a velocity. The Brunt-Väisälä frequency is:

$$N = \sqrt{-(g/\theta_0)\partial_z \bar{\theta}} \,, \quad (3)$$

and $f = 2\Omega$ is twice the rotation frequency; $\nu = \kappa$ are the kinematic viscosity and the thermal diffusivity. Temperature and density fluctuations are related through $\rho = \rho_0 + z\partial_z \bar{\rho} + \rho'$, $\rho' = \theta N \rho_0 / g$, with g the acceleration of gravity, ρ_0 a uniform density and $\partial_z \bar{\rho} < 0$ the imposed vertical gradient.

The maximum wave number of the computations is $k_{\max} = n_p/3$ with a truncation performed in order to eliminate aliasing errors in the Geophysical High-Order Suite for Turbulence (GHOST) code. This code is pseudo-spectral and parallelizes using a hybrid methodology [26]; it now demonstrates scalability to in excess of 130000 compute cores. The set of primitive equations in GHOST encompasses fluids with or without rotation and stratification, as well as MHD with or without a Hall current. GHOST also contains several parameterization schemes such as the Lagrangian-averaged (alpha) model [27] and its variants (see, *e.g.*, [28,29]).

The velocity field is taken initially as isotropic and at large scale; its spectrum is centered on k_0 with $k_0 \in [2, 3]$. There are no initial temperature fluctuations, but they develop fast, through wave exchanges. This choice was also taken in [30]; it allows for buoyancy fluctuations to develop from the internal dynamics of the Boussinesq equations. In the absence of forcing, no inverse cascade of energy is expected, so that these large-scale initial conditions are best suited to enhance the Reynolds number at a given resolution and observe the formation and role of density fluctuations *ab initio* (see [31] for a study of RST forced at large scales). Such a choice of initial conditions is traditional in the turbulence community and allows us to contrast the evolution of different flows for a large set of parameters, including some close to homogeneous isotropic turbulence (when both Fr and Ro are larger than unity).

Considering the ratio of relevant time scales in the problem associated with nonlinearity, dissipation, as well as the rotation and stratification periods, it is well known that one can define the following three dimensionless parameters (the Prandtl number $Pr = \nu/\kappa$ having been set equal to unity):

$$Re = \frac{U_0 L_0}{\nu}, \quad Ro = \frac{U_0}{f L_0}, \quad Fr = \frac{U_0}{N L_0} \,, \quad (4)$$

namely the Reynolds, Rossby and Froude numbers, with U_0 and L_0 characteristic velocity and length scales. The buoyancy Reynolds number is defined as

$$\mathcal{R}_B = ReFr^2 = [L_{Oz}/\eta]^{4/3} = [L_0/\eta]^{4/3} * [L_B/L_0]^2 \,, \quad (5)$$

with $L_B = U_0/N$, $L_{Oz} = [\epsilon_V/N^3]^{1/2}$ and $\eta = [\epsilon_V/\nu^3]^{-1/4}$ the so-called buoyancy, Ozmidov and Kolmogorov scales respectively; here, $\epsilon_V = DE_V/Dt$ is the kinetic energy dissipation rate (see below, eq. (9)). $\mathcal{R}_B$ can be viewed as either a small-scale Froude number [32], or a small-scale, effective Reynolds number. Finally, the Burger and Richardson numbers are defined as

$$Bu = Ro/Fr, \quad Ri = \frac{N^2}{\langle [\partial_z u_\perp]^2 \rangle}\,. \tag{6}$$

The Burger number measures the relative strength of stratification and rotation and can vary from a few in the ocean up to in excess of 100 in the atmosphere; it is evaluated at the peak of dissipation. Note that several definitions can be found for the Richardson number; in the absence of imposed large-scale shear S, we have chosen to take for shear the volume-averaged vertical gradient of the horizontal velocity, $u_\perp = \sqrt{|u_x|^2 + |u_y|^2}$.

Kinetic and potential energies are defined as usual:

$$E_V = \frac{1}{2}\int \|\mathbf{u}(\mathbf{x})\|^2 \mathrm{d}^3\mathbf{x}, \tag{7}$$

$$E_P = \frac{1}{2}\int |\theta(\mathbf{x})|^2 \mathrm{d}^3\mathbf{x}, \tag{8}$$

with the total energy $E_T = E_V + E_P$. Their respective dissipation rates are:

$$\epsilon_V = \nu \int \|\boldsymbol{\omega}(\mathbf{x})\|^2 \mathrm{d}^3\mathbf{x}, \quad \epsilon_P = \kappa \int \|\nabla\theta(\mathbf{x})\|^2 \mathrm{d}^3\mathbf{x}, \tag{9}$$

with $\boldsymbol{\omega} = \nabla \times \mathbf{u}$ the vorticity, and with $\epsilon_T = \epsilon_V + \epsilon_P$ the total dissipation in the flow.

The large parametric study that is analyzed in this paper, with a total of 65 runs, covers the following ranges (see table 1): $1984 \leq Re \leq 18586$ (with ν varying from 10^{-4} to 5 times that), $10^{-3} \leq Fr \leq 5.5$ (with $0.01 \leq \mathcal{R}_B < 1.3 \times 10^5$), $0.11 \leq Ro \leq 42$ and $2.47 \leq N/f \leq 312$. Time steps are either 4×10^{-4} or 7.5×10^{-4}, according to Reynolds number. The Reynolds numbers are low for geophysical flows, except for the Mesosphere and Lower Thermosphere (MLT), but this limitation is due to the fact that in a direct numerical simulation, all scales must be resolved down to the dissipation scale. The Burger number also covers a large span in values; indeed, in the ocean, stratification is strong and Bu can be rather small (≈ 5 or 10) whereas in the atmosphere, the flows go from being strongly stratified and strongly stable in the nocturnal planetary boundary layer (PBL) to fully convective. A weak rotation run ($Ro = 920, N/f = 13750$, run 30), and a few purely stratified cases (with $f = 0$, runs 62–65) are also included in the analysis; they can be viewed as the limiting case when rotation is negligible, such as at the Equator. The resulting buoyancy Reynolds numbers vary from less than unity to in excess of 10^4.

3 Results

3.1 Overall structures

Stratified flows develop thin layers, whereas rotating flows support vertical (Taylor) columns. In the presence of both rotation and stratification, complex structures are observed for various values of N/f in DNS (see *e.g.*, [33–35]). Figures 1 and 2 display the temperature fluctuation (scalar) field and the norm of its gradient respectively. These are visualized at the peak of the total dissipation for a run with $N/f = 137$, $Fr = 0.067$, $Re = 11723$; thus $Ro \approx 9$ and $\mathcal{R}_B \approx 53$ (run 31 of table 1). These parameters correspond to the MLT [36] for which the Reynolds number is of order 10^4, close to the DNS value. We note that positive and negative temperature fluctuations alternate in rather thick layers that have convoluted contour lines because of localized small-scale instabilities. The resulting gradient field displays intense dissipation regions (see for example the lower right corner, following the direction of the red arrow to the end of the cube). These regions are in fact quite extended, and are contiguous to low dissipation regions, a classical feature of intermittency which is known to develop in wave turbulence [37–40].

Thus, the vertical buoyancy flux $\langle \theta w \rangle$ is subject to wide variations due to the sporadic and intermittent nature of the transient events giving rise to it, such as frontogenesis [41,6], Kelvin-Helmoltz overturning events and breaking of nonlinear waves. Strong variability is well-known in the nocturnal planetary boundary layer [42], as well as in the ocean [43], and this intermittency can be modeled simply through a competition between advection and buoyancy in the Boussinesq equations [40].

3.2 Temporal evolution

We plot in fig. 3 (left) the temporal evolution for three subsets of runs of the kinetic energy (and its dissipation in the inserts), whereas in the right column of fig. 3, we display for the same three sets of runs the time variation of the total energy and in the inserts, the ratio of the kinetic to potential energy. The top of these two figures relate to runs with approximately constant and low Rossby number and small Froude number (although it varies by roughly a factor 10). In the middle plots, by contrast, Fr is constant and small (and thus so is $\mathcal{R}_B$), with Ro varying by a factor of 20. Finally, in the bottom plots, Fr is again approximately constant but significantly higher, and $\mathcal{R}_B$ is higher also, with now Ro varying by a factor of 8. For all these runs, the turn-over time $\tau_{NL} \approx 3$ in the units displayed in the figures. These runs correspond respectively, when referring to table 1, to Id= 3, 9, 13, 17 and 27 (top figures), Id= 31, 33, 34, 36 and 38 (middle figures) and Id= 46, 48, 49, 50 and 54 for the bottom figures, all Id numbers being given by ascending Froude number. The Burger number varies between 2.5 and 20 for the top plots, 5 and 137 for the middle plots and between 25 and 199 for the bottom plots. As such, this selection of 15 runs represents a thorough sample of the data base.

Table 1. Parameters of the DNS simulations identified by Id; all are performed on cubic grids of 1024^3 points in the absence of forcing and with periodic boundary conditions. Initial conditions are isotropic and random for the velocity field only, and they are centered in the large scales, with $L_0 \approx 2.5$. Re, Fr and Ro are the Reynolds, Froude and Rossby numbers computed at the time of maximum of enstrophy for each run. Derived parameters of interest are the buoyancy Reynolds number $\mathcal{R}_B = ReFr^2$ and the Burger number $Bu = Ro/Fr$, for a cubic box; they are also evaluated dynamically, at peak of dissipation. Runs are ordered by their Froude number, and horizontal lines are simply to guide the eye. Lowest and highest Re are for runs 54 and 23, lowest and highest $\mathcal{R}_B$ are for runs 1 and 61, whereas lowest and highest values of Ro/Fr are for runs 52 and 14, respectively. Low Burger numbers correspond to the ocean, whereas high values correspond to the atmosphere and the MLT. Note that all computations except for runs 58-61 have $Fr < 0.62$ and $\mathcal{R}_\mathcal{B} < 1900$; also note that run 30 has a very high Rossby number, and that the last four runs (62–65) are purely stratified, with the rotational frequency $f = 0$.

Id	Fr	Ro	Ro/Fr	Re	$\mathcal{R}_B$	–	Id	Fr	Ro	Ro/Fr	Re	$\mathcal{R}_B$
1	0.00129	0.12952	100.15	10905	0.01824		34	0.08839	0.61873	7	8525.4	66.61
2	0.002307	0.11535	50	9895.3	0.05267		35	0.09211	4.6056	50	11016	93.47
3	0.006078	0.12038	19.805	10678	0.39452		36	0.09902	9.2829	93.75	7717.1	75.66
4	0.006421	0.63255	98.507	9270.5	0.38225		37	0.09911	6.8828	69.444	7717.9	75.81
5	0.007347	0.22532	30.667	13945	0.75279		38	0.09989	0.49448	4.9502	8200.5	81.83
6	0.01165	0.30505	26.182	14679	1.9927		39	0.10038	9.411	93.75	10747	108.3
7	0.01192	2.9804	250	13504	1.9192		40	0.1007	6.993	69.444	10754	109.05
8	0.01271	0.63538	50	8933.1	1.4425		41	0.10167	7.0606	69.444	16226	167.73
9	0.02098	0.14679	6.9963	11079	4.8773		42	0.13318	0.32923	2.472	7563.2	134.15
10	0.02150	0.46444	21.6	13449	6.2177		43	0.13614	0.67308	4.944	7603.2	140.92
11	0.02253	0.11157	4.95	10977	5.57		44	0.14014	0.98247	7.0106	7442.2	146.16
12	0.02618	4.5819	175	12044	8.26		45	0.14222	1.4063	9.8881	7327.7	148.22
13	0.02800	0.14002	5	10722	8.41		46	0.16318	9.791	60	9576.1	255
14	0.03015	9.4215	312.5	10522	9.56		47	0.18841	37.481	198.94	2520.7	89.48
15	0.03332	4.5814	137.5	13020	14.45		48	0.20152	5.0381	25	8718.2	354.06
16	0.03646	9.1153	250	13217	17.57		49	0.20159	10.08	50	8756.8	355.87
17	0.03774	0.13994	3.708	10534	15.00		50	0.2059	40.96	198.94	6272.1	265.89
18	0.04094	0.60719	14.832	9842.9	16.50		51	0.25825	10.33	40	8575.7	571.95
19	0.04221	0.21106	5	14841	26.44		52	0.34081	0.84249	2.472	5024.4	583.59
20	0.04527	3.0177	66.67	12790	26.21		53	0.37971	11.391	30	7116.6	1026.1
21	0.04737	4.4406	93.75	8881.9	19.93		54	0.3966	42.192	106.38	1983.7	312.03
22	0.04803	4.5028	93.75	12366	28.53		55	0.46877	1.1719	2.5	4500.4	988.95
23	0.04870	4.5657	93.75	18586	44.08		56	0.55387	11.077	20	7138.8	2190
24	0.04897	9.1824	187.5	18550	44.49		57	0.61542	1.5386	2.5	5012.1	1898.3
25	0.04940	9.2627	187.5	12769	31.16		58	0.89372	2.2343	2.5	4707.8	3760.3
26	0.05656	0.28278	5	13730	43.92		59	1.2497	12.497	10	6473.2	10110
27	0.05679	0.1404	2.472	9747.6	31.44		60	2.6918	13.459	5	4019.3	29123
28	0.060595	3.0297	50	11649	42.77		61	5.4829	13.707	2.5	4257.7	1.28×10^5
29	0.062114	0.61418	9.8881	9639.4	37.19		–					
30	0.066925	920.23	13750	11486	51.45		62	0.01212	Inf	Inf	15225	2.24
31	0.06715	9.2332	137.5	11728	52.88		63	0.02678	Inf	Inf	11804	8.46
32	0.073074	3.0448	41.667	12211	65.20		64	0.06692	Inf	Inf	11487	51.44
33	0.08608	0.4304	5	12111	89.74		65	0.20147	Inf	Inf	8796.7	357.07

With the time axis in units close to the eddy turnover time, the first thing to notice is that the smaller the Froude number is, the faster the oscillations due to inertia-gravity waves, and the less effective the decay of energy is, as one can expect in a weak turbulence regime in which the strong waves impede the nonlinear energy transfer to small scales. One can note that for high Rossby number and exactly the same Froude number $Fr = 0.202$, temporal evolutions are identical (runs 48 and 49), whereas when comparing runs 36 and 38 both with $Fr = 0.099$ and Ro differing by a factor of ≈ 20, time variations remain close but not identical: indeed, for low Ro, the influence of the rotation on the dispersion relation that governs the characteristic time of the waves is felt even when examining integrated quantities such as the energy. Its influence is also visible on how slanted structures are, and a study of

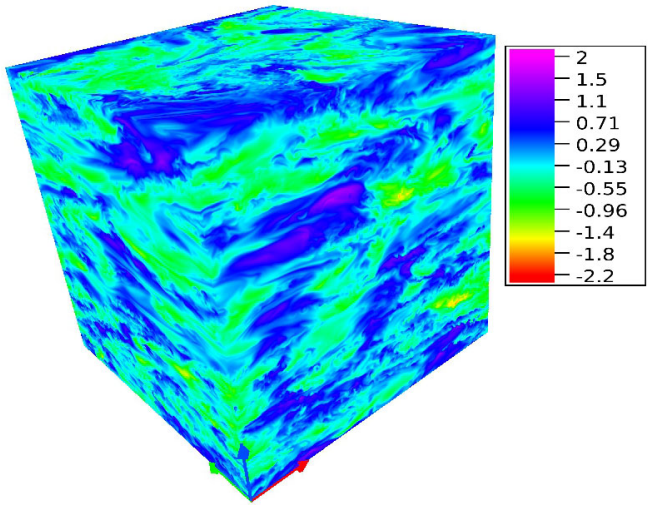

Fig. 1. Visualization of temperature fluctuations at the peak of dissipation for a run with $N/f = 137$, $\mathcal{R}_B = 53$ (run 31 of table 1) corresponding to conditions in the Mesosphere and Lower Thermosphere (MLT), using a linear color scale (see inset). The common direction of gravity and rotation is given by the vertical (blue) arrow.

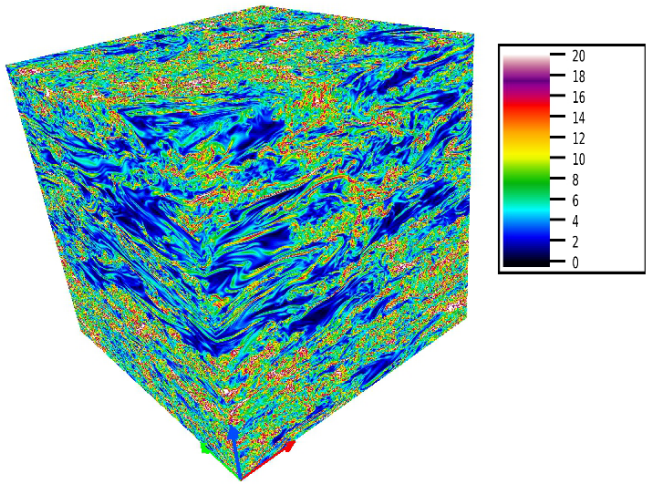

Fig. 2. Visualization of the magnitude of the gradient of temperature fluctuations at the peak of dissipation for the same MLT run as in fig. 1 with $N/f = 137$, $\mathcal{R}_B = 53$, using again a linear color scale (see inset).

the anisotropy of such flows (see [35] for the forced case in the inverse cascade regime) will be performed in the future; note that anisotropy can persist at high Reynolds numbers when looking at high-order moments, as found for example in [44] for shear flows.

Another striking result of these plots is the evolution of the enstrophy: for all runs but one (for which the Froude number is the lowest, ≈ 0.006, run 3), the kinetic energy dissipation peaks at the same time ≈ 5, an indication that nonlinear coupling between inertia-gravity waves and eddies is governing the small-scale dynamics: the more dissipation the weaker the waves (fig. 3, middle), whereas for higher Fr, $\mathcal{R}_B$ and Ro, the amount of energy dissipated by the velocity field is approximately constant although such is not the case for the potential field which becomes negligible (but has a plateau when normalized by the potential energy, see fig. 5 below).

Finally, for most of the runs as seen in fig. 3, the ratio of kinetic to potential energy stays in a range close to 4. It is only for the three runs at the highest $\mathcal{R}_B$ that this ratio abruptly increases, indicative of a change in the dynamics of the flow, also observed in figs. 5, 6 and 7 below.

Thus, we now move on to a more systematic study of the dynamics of the RST flows covered by our computations, examining specifically the different modes of energy and their respective dissipation rates as a function of dimensionless parameters.

3.3 The apparent lack of role for rotation on kinetic-potential global dynamics

As stated before, in this study, the Rossby number varies from 0.11 upward: the effect of Earth's rotation depends

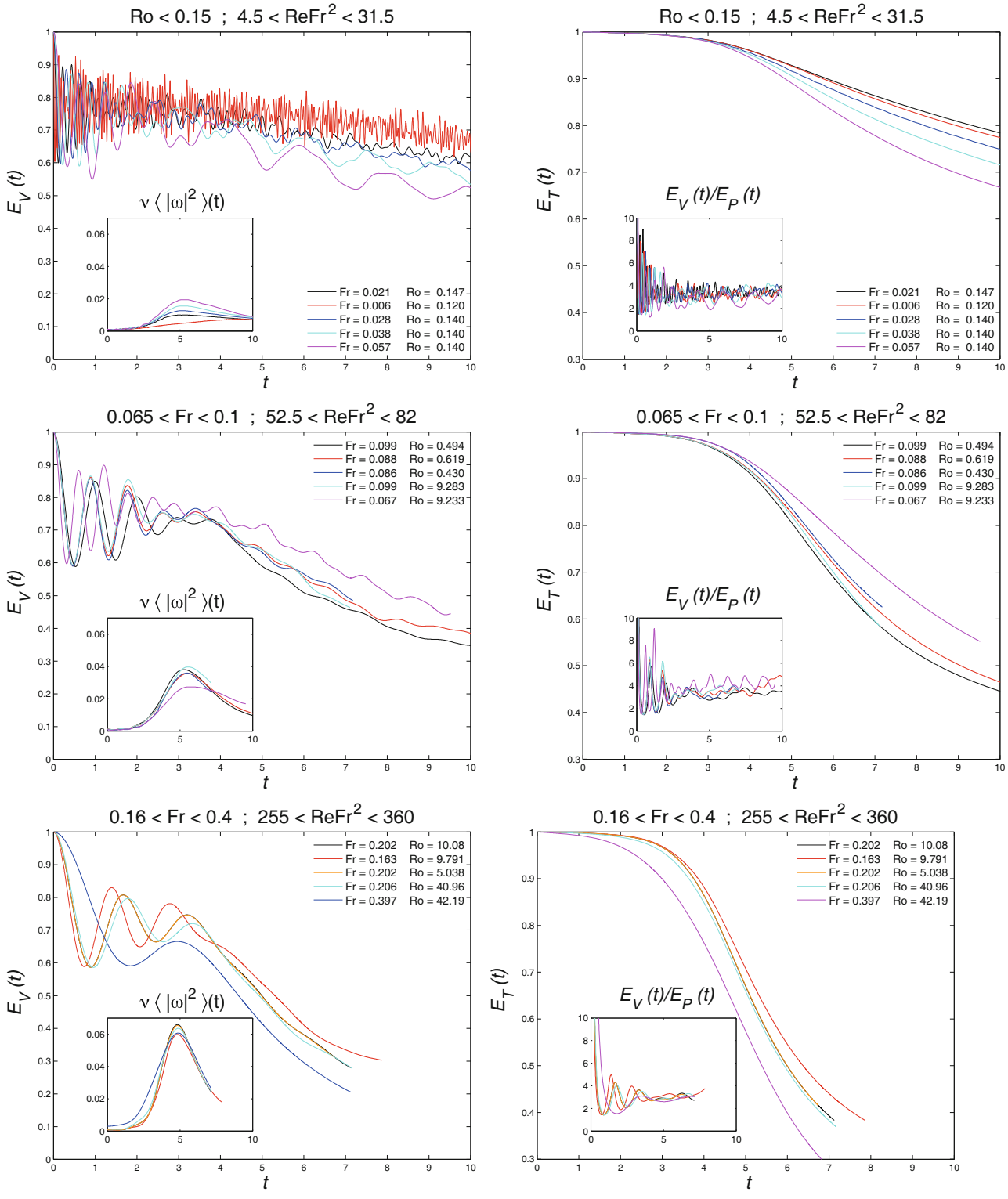

Fig. 3. Left: Temporal evolution of kinetic energy (and of its dissipation in the insert) for three sets of runs. Top: Constant and low $Ro < 0.15$, with $Bu = Ro/Fr$ varying between ≈ 2.5 and 20; runs ID are 3, 9, 13, 17 and 27 in ascending Froude number (see table 1). Middle: Relatively constant Fr at low values, with resulting moderate $\mathcal{R}_B$ ($0.065 < Fr < 0.1$, $50 < \mathcal{R}_B < 100$, runs 31, 33, 34, 36 and 38). Bottom: Same as above but with higher Fr and $\mathcal{R}_B$ ($0.16 < Fr < 0.4$, $200 < \mathcal{R}_B < 400$, runs 46, 48–50, 54). Right: Evolution of the total energy and of the ratio of kinetic to potential energy in the insert, for the same runs as in the left column. Note the relatively constant E_V/E_P ratios throughout the runs with rather different parameter values, as it settles at the time of maximum dissipation, after initial oscillations due to the early dominance of the waves.

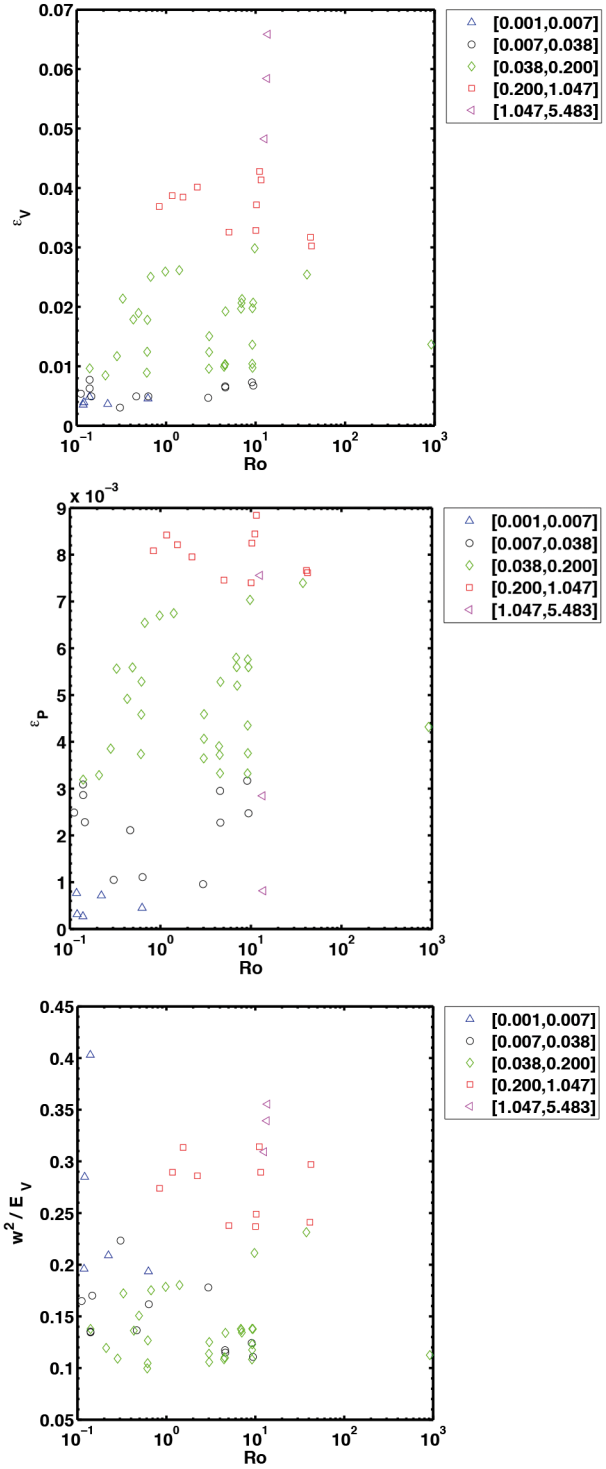

Fig. 4. Kinetic (top) and potential (middle) dissipation rates ϵ_V, ϵ_P as a function of Rossby number. Bottom: Vertical to total kinetic energy ratio E_z/E_V (with $E_z = \frac{1}{2}\langle w^2/2\rangle$) as a function of Ro. Different symbols and colors identify bins in Froude numbers (see inserts), each with a variation by approximately a factor of four.

on latitude and inertial waves are more important at mid to high latitudes. We show in fig. 4 the variation of the kinetic energy dissipation rate ϵ_V with Ro (top), that of the potential energy dissipation rate ϵ_P with N/f (middle) and of the ratio of vertical to total kinetic energy again with Ro (bottom). Here, symbols/colors identify bins in Froude number, whereas in figs. 5, 6 and 7 they identify bins in Ro. For different Ro and N/f, identical values of dissipation or of vertical energy E_z are measured for Fr bins, although at a given Ro (or N/f), these values depend on how strongly stratified the flows are. Thus, in all cases, a large scatter in the data is obtained with order-of-magnitude variations of the dissipation rates at a fixed value of parameters (Ro or N/f), and with no discernible trend. Note also that the potential energy dissipation rate is always smaller than that for kinetic energy, as expected. We can conclude from these plots that neither the absolute magnitude of the rotation, measured by the Rossby number itself, nor its relative strength compared to the stratification, as quantified by the Burger number, plays a role: the small-scale energy that leads to dissipation is dominated by the strength of the imposed stratification, possibly simply because $N/f > 1$ for all these runs. However, it is well known that rotation plays an important role at large scale in the presence of forcing (see sect. 4), and that it may also be the case when examining the slow-fast mode energetic partition [45,46] (see also sect. 4). We should also note that the Rossby number in the present data base is never very small, with a minimum ≈ 0.1.

3.4 Time scales associated with kinetic-potential energy exchanges

The temporal as well as spatial burstiness of the flow renders difficult an evaluation of transport coefficients on longer time scales as occur in climate. When it is not possible to perform long averages, as in decaying turbulence, other means of measuring small-scale properties have been constructed, for example following the Lagrangian dynamics of the flow [30,47,48] (see also [49] for convectively unstable boundary-layer flows). These properties are associated with kinetic and potential energy exchanges, globally and among scales, and between the underlying waves and nonlinear eddies, rendering interpretation difficult as the small-scale dynamics may depend on both the global and local parameters of a given flow at a given time.

Thus, in further understanding how energy is distributed between these modes, it is customary to define γ, a time scale ratio based on kinetic and potential energy, $E_{V,P}$ and their dissipations, $\epsilon_{V,P}$, namely:

$$\gamma = \frac{T_V}{T_P} = \frac{E_V}{\epsilon_V}\frac{\epsilon_P}{E_P}\,, \qquad (10)$$

T_V and T_P are dimensional evaluations of the time it takes in a given flow to dissipate its kinetic and potential energies. As such, they give a measure of the effective dissipation that can occur in such flows submitted to both linear waves and nonlinear turbulent transfer to small scales. Note that measuring T_V can yield immediately the Taylor scale defined as $\lambda \sim \sqrt{\nu E_V/\epsilon_V}$ (with the associated Taylor Reynolds number $R_\lambda = U_0\lambda/\nu$, see *e.g.* [50]). One readily derives that $T_V = \lambda^2 Re/[U_0 L_0]$ and

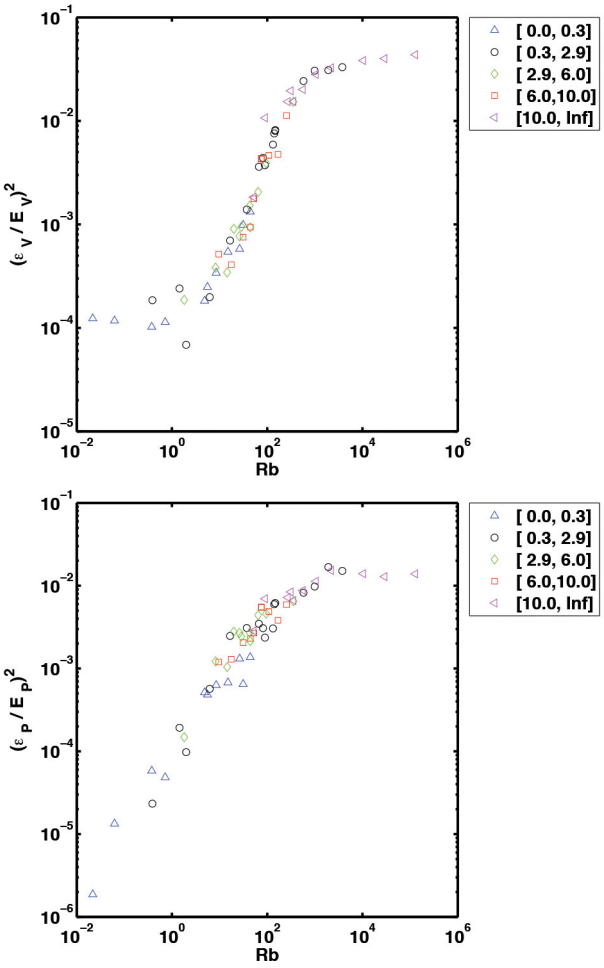

Fig. 5. Time scale variations: T_V^{-2} (top) and T_P^{-2} (bottom) as a function of buoyancy Reynolds number $\mathcal{R}_B$, with $T_V = E_V/\epsilon_V$ and $T_P = E_P/\epsilon_P$ as defined in eq. (10). Data is binned as in fig. 4, but using now the Rossby number Ro (see inserts).

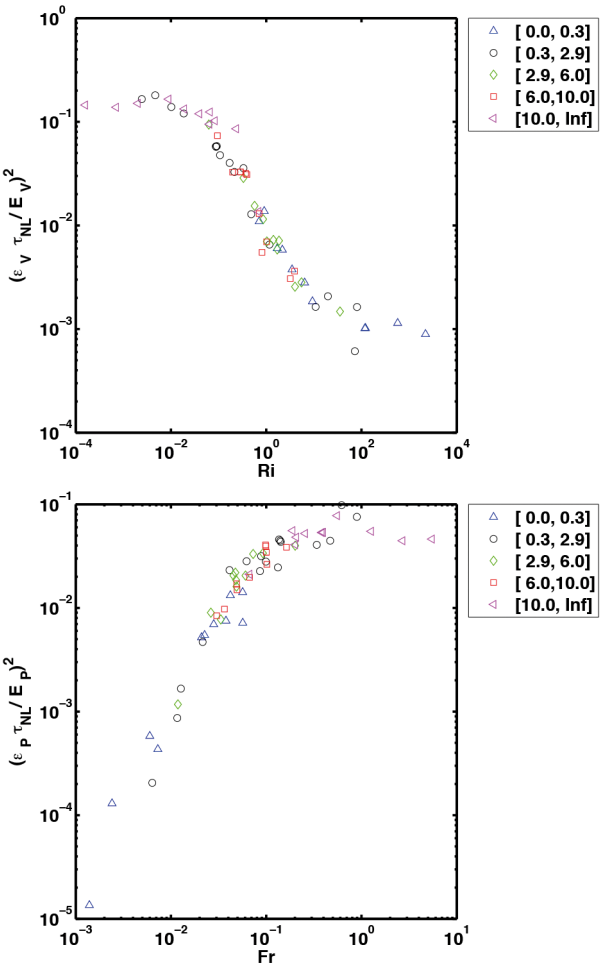

Fig. 6. Top: $[\tau_{NL}/T_V]^2$, as a function of Richardson number. Bottom: Same as above, for the time associated with the temperature field, $[\tau_{NL}/T_P]^2$, as a function of Froude number Fr (see eq. (10)). The binning is done in Ro as in fig. 5.

$R_\lambda^2 = U_0 T_V Re/L_0$. With T_V being found in a range ≈ 5 to 100 according to fig. 5 (see below), we can immediately deduce that R_λ varies from roughly 200 to 800 for this parametric study, with higher R_λ at lower Froude numbers because T_V is larger or equivalently ϵ_V is smaller, as in weak turbulence for which $\epsilon_V = \epsilon_D Fr$. In that case, $R_\lambda = \sqrt{Re/Fr} = L_0/\ell_N$ where $\ell_N = \sqrt{\nu/N}$ is a length scale associated with the thickness of the vertical layers. Finally note that the total energy and its dissipation, E_T and ϵ_T, can also be used to define γ (instead of E_V, ϵ_V) as done in [30]. The two definitions may not result in very different estimates since both the dissipation and, to a lesser extent the energy, are dominated by the velocity field except at high Richardson numbers.

A word of caution here is that T_V is not necessarily equal to the eddy turn-over time $\tau_{NL} = L_0/U_0$ since, in a weak turbulence regime, the energy dissipation rate may be smaller than the Kolmogorov (dimensional) estimate ϵ_D by a factor proportional to the Froude number for stratified flows and to the Rossby number for rotating flows [17]. Furthermore, the ratio γ can be related to the instantaneous scalar turbulent diffusivity $\kappa_{\rm turb}$ in the following way:

$$\kappa_{\rm turb} = \kappa \langle \|\nabla\theta\|^2 \rangle / [\partial_z \bar{\theta}]^2 = \gamma L_E^2 / T_V, \qquad (11)$$

with L_E being the (vertical) Ellison scale; it is defined as $L_E^2 = E_P/[\partial_z \bar{\theta}]^2$, where $\partial_z \bar{\theta}$ is related to the Brunt-Väisälä frequency (see eq. (3)). Thus, L_E is a scale similar to a mixing length but now associated with the vertical variations of density or temperature fluctuations. It is found to be useful in analyzing oceanic data for example, since it can be directly measured in turbulent flows, thus allowing for a determination of the energy dissipation rate, a key ingredient in the dynamics of rotating stratified turbulence.

The variation of the relative anomalous scalar diffusivity $C_\kappa = \kappa_{\rm turb}/\kappa$, also called the Cox number, with the buoyancy Reynolds number is known to display several regimes in terms of $\mathcal{R}_B$ [51,52]. Here, anomalous is meant in the sense that the Cox number can differ from unity, or in other words the dissipation can be enhanced by nonlinear coupling of waves such as when the vortical mode plays

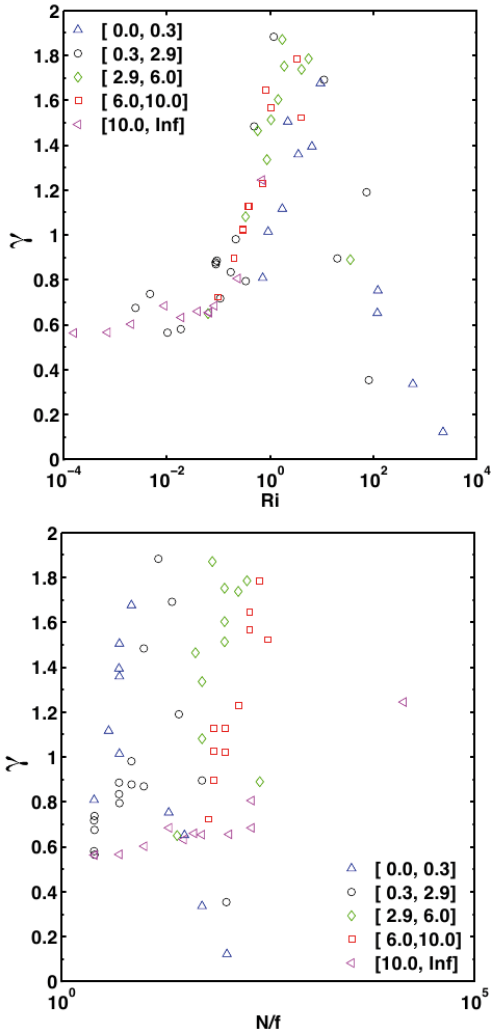

Fig. 7. Time scale ratio $\gamma = T_V/T_P$ (see eq. (10)) as a function of Ri (top) and of N/f (bottom). Binning in Ro as in fig. 5.

the role of a catalyst for the wave modes to transfer energy to small scales (see *e.g.* [53]). In [47], variations of C_κ with parameters are attributed to the variation of T_V and L_E with the level of stratification, and with γ itself staying relatively constant in the range of parameters studied, for $1 < \mathcal{R}_B < \infty$, but with Taylor Reynolds numbers of at most 90, whereas in our study they are roughly up to ten times larger.

The conclusion in [47] of the constancy of γ throughout a large range of parameters may be pointing to a self-adjustment of stratified flows whereby the difference in (large-scale) energy distribution is compensated by small-scale activity such that the time scale ratio (γ) remains constant, a conclusion which is at odds, however, with (quasi-) equipartition ideas ($E_V \approx 2E_P$ in some range of scales), as emphasized on a phenomenological basis for example in [54] (see also [55]). The idea of equipartition of kinetic and potential energy at small-scale has been backed up recently, in the context of the shallow water model, by theoretical arguments based on statistical mechanics: at statistical equilibrium, the kinetic and potential energy of the small-scale fluctuations are equal [56], in fact as expected for a linear wave.

Therefore, using the database summarized in table 1, we are now investigating whether the characteristic times and their ratio, γ, remain relatively constant with parameters or not. We show first in fig. 5 the variations of the two time scales directly associated with the problem of rotating stratified turbulence, namely we plot $[\epsilon_V/E_V]^2 = T_V^{-2}$ (top) and $[\epsilon_P/E_P]^2 = T_P^{-2}$ (bottom) as a function of buoyancy Reynolds number. First, at low $\mathcal{R}_B$, *i.e.* for strong waves, T_P grows rapidly because E_P grows from zero, its initial condition. On the other hand, T_V has a plateau up to $\mathcal{R}_B \approx 1$, at which value turbulence comes to set in at small scales: for $\mathcal{R}_B = 1$, the Ozmidov scale (see eq. (5)) becomes equal to the (Kolmogorov) dissipation scale η, and isotropy is thought to recover for $\ell < \ell_{Oz}$ when resolved *i.e.* for $k_{\max} > 2\pi/\ell_{Oz}$. We observe similar variations in both figures for intermediate values of $\mathcal{R}_B$. As the turbulence increases in strength, *i.e.* for higher values of the buoyancy Reynolds number, T_V and T_P both become shorter; this corresponds to more efficient transfer of energy to small-scales as expected for nonlinear wave coupling, and thus to more dissipation. Finally, at high $\mathcal{R}_B > 10^3$, a plateau is reached for both time scales, indicative of a lesser role of the waves with turbulence governing now the evolution of the flow.

Note also that for low values of $\mathcal{R}_B$, the T_V and T_P time scales associated with the effective dissipation of the velocity and the potential temperature fluctuations have a different behavior. This could be attributed to the fact, as stated before, that initially there are no temperature fluctuations; thus, potential energy is created because of its (linear) interactions with the velocity field through the buoyancy terms. On the other hand, when the waves are strong (low $\mathcal{R}_B$), the time scale for the velocity field, T_V, remains constant (to a value likely determined by initial conditions and Froude and Rossby numbers).

When we now normalize the velocity time scale T_V by the eddy turn-over time, we see that T_V is indeed not equal to τ_{NL}, with a ratio between these two time scales varying strongly with Richardson number (see fig. 6, top). A similar (but opposite) variation is observed when plotting the same data as a function of $\mathcal{R}_B$ (not shown).

What the plots in fig. 6, indicate is that the actual dissipation times, measured by $T_{V,P}$, are longer than what dimensional analysis would give for homogeneous isotropic turbulence at high Reynolds number, namely the turn-over time τ_{NL}. The (relative) acceleration of the weak turbulence (larger $\tau_{NL}/T_{V,P}$, see fig. 6) as the Froude number grows is compatible with a linear variation: at fixed τ_{NL}, as stratification weakens, the mode-to-mode transfer of energy to small scales is more efficient, *i.e.* faster. Concerning the time based on potential energy and its dissipation, there is a rather flat dependence of this time scale ratio with Froude number with a threshold at $Fr \approx 0.4$.

The same normalization by the turn-over time but now examining the temperature field displays a comparable behavior, as shown in fig. 6 (bottom), where it is plotted as

a function of the Froude number. Note that the interplay between kinetic and potential energy is also studied in [57] for forced stratified turbulence in a thin layer of fluid. They find that in the presence of stratification, the large-scale flux of energy due to rotation is reduced, and that the rate of dissipation of potential energy grows with Froude number, as also indicated in fig. 6 (bottom).

The combination of these phenomena can be embedded in the expression for $\gamma = T_V/T_P$ which is shown in fig. 7 as a function of the Richardson number Ri (top), and of N/f (bottom). The bell-shape of the γ variation with Richardson number is associated with the fact that the plateaux in T_V and T_P occur for different values of Ri (and of $\mathcal{R}_B$), and that the saturation is smoother in T_P. Plotted against buoyancy Reynolds number, the evolution is similar, again with a bell-shaped curve (not shown) that mirrors that for the Ri variation. Note that for turbulent flows (low average Ri), the ratio of velocity and potential time scales is close to unity, indicative of strong mixing. We see finally in fig. 7 (bottom), as already stated in the context of fig. 4, that N/f is not a determining parameter for γ either: γ can vary by one order of magnitude at a given N/f, and for all N/f values explored in this paper (except for the highest one for which only one run was performed). The low values of γ at high Richardson numbers may be linked to the fact that these runs are performed with zero initial conditions in the temperature fluctuations. Note that the binning in these figures enhances the fact that, as noted before, weak (*vs.* strong) turbulence in terms of both Ro and Fr, correspond to large (*vs.* small) $T_{V,P}$. In a Kolmogorov regime for purely stratified turbulence, the energy spectra in terms of $k_\perp$ (referring to the direction of gravity) are thought to be $E_V(k) \sim \epsilon_V^{2/3} k_\perp^{-5/3}$ and $E_P(k) \sim \epsilon_P \epsilon_V^{-1/3} k_\perp^{-5/3}$ [58], with in this case the temperature fluctuations following a passive scalar scaling, the buoyancy terms in the Boussinesq equations being now sub-dominant when compared to nonlinear advection. Such a scaling implies that $\gamma = T_V/T_P = [\epsilon_V/E_V]^{-1}\epsilon_P/E_P] = 1$ within a constant of order unity, a balance that is reached at all scales in that regime. Examining fig. 7, we find that this is the case at small Richardson number when the flow is almost everywhere unstable, whereas it ceases to be the case for $Ri \geq 0.1$, or in terms of buoyancy Reynolds number, for $\mathcal{R}_B \leq 100$. By analogy with the study of purely stratified turbulence as performed in [58], one thus could say that in rotating stratified turbulence, the fully turbulent regime may be obtained for $\mathcal{R}_B > 100$.

Our conclusion is that, for the parametric study analyzed in this paper, γ displays strong variations with parameters. However one should note that in [59] a temporal integral of the dissipation is performed over a period of ten turn-over times, covering an ensemble of overturning events whereas in the present paper we compute the time scale ratio γ at the time of the peak of dissipation. Furthermore, the variation of γ we observe is by a factor ≈ 3 when considering intermediate values of Ri (namely $Ri < 10$), roughly twice as large as the strong intermittent temporal fluctuations that are found in [30] over $10\tau_{NL}$.

4 Discussion and conclusions

We have performed in this paper a preliminary analysis of the data base created for rotating stratified turbulence in the absence of forcing and for a wide range of values of the dimensionless parameters governing the evolution of such flows. We find a substantial variation with parameters of the characteristic time scales, with a plateau in $\gamma \approx 0.6$ starting for $Ri \leq 0.1$. Note that, in the context of a study of the instability of a baroclinic eddy in the atmospheric mesoscales, a detailed analysis of the properties of the nonlinear and kinetic transfer times has been reported in [60] where it is shown as well that there is a wide variation in these times with altitude, and thus with stratification, when going from the upper troposphere to the lower stratosphere.

Our analysis also leads to the conclusion that, at small scale, rotation has no overall dominant effect, except in the development of structures that are not simply horizontal layers as in the purely stratified case. However, there is evidence for a kink associated with rotation in the slow-mode spectra in forced RST computations performed recently [45], a kink also observed in [46] at sufficiently high Reynolds numbers in the decaying case.

Furthermore, rotation is known to have an influence on the inverse cascade to large scales in the presence of forcing, including in laboratory experiments [61]. Critical Rossby numbers for the inverse cascade to stop occurring can be found in the literature to be between ≈ 0.1 [62] or 0.2 [63] and up to ≈ 0.45 [64], whereas, in terms of micro-Rossby number $R_\omega = \omega_{\text{r.m.s.}}/f$ where $\omega_{\text{r.m.s.}}$ is the r.m.s. vertical vorticity, the transition is found to be for $R_\omega < 3$ [65]. Also, N/f which does not seem to play a role in the present study, is however the relevant parameter when examining the relative strength of the inverse and direct constant energy fluxes [64], so that the effect of rotation is indeed mostly felt in the large scales and in the presence of forcing (see also [57]). There is no inverse cascade of energy in purely stratified flows, although wave interactions do produce a measurable inverse transfer of energy to large scales, but with a flux that becomes negligible when the Reynolds number is increased and with no measurable growth of total energy (see for example [66,63,67,68]). However, in the present computations with large-scale initial conditions and no forcing, any such effects due to rotation are, in essence, strongly blocked.

In [69], purely stratified flows are studied for long times. Results show a strong difference in the behavior of helicity (velocity-vorticity correlations) in the case of a Beltrami (fully helical) initial condition: total helicity increases with time for Froude numbers below unity, and this corresponds to a relative helicity that reaches close to maximum values associated with an alignment (or anti-alignment) between velocity and vorticity (see also [70]). It will be of interest to study the variation in the behavior of helicity with parameters. Indeed, helicity can be created by rotating stratified flows [71], in particular when waves are strong (with $\mathcal{R}_B < 20$) [72] and it can affect the

rate at which energy decays, as shown in [24] for rotating flows, and in [70,69] for stratified flows.

Future investigations will be concerned with a study of the mixing efficiency in these flows in terms of flux Richardson number as used mostly in the oceanographic context (see, *e.g.* [52] for review) [73], and spectral properties of kinetic and potential energies and their fluxes, as well as slow (vortical) and fast (wave) modes, both in isotropic and anisotropic terms. Furthermore, a better assessment of the dynamical time scales of such flows will be obtained by taking into consideration several other effects, such as what is the role of i) examining different initial conditions, for example balanced flow between velocity and temperature fluctuations (see *e.g.* [74]); ii) resolving or not the Rossby deformation radius L_D which can be seen as the scale at which there is a balance in the dispersion relation of inertia-gravity waves between gravity and rotation, *i.e.* between the development of small scales in the parallel and perpendicular directions (namely $L_D \sim \frac{N}{f} L_z$ with L_z a characteristic vertical scale, with the directions referring to that of rotation and gravity); and iii) forcing at relatively small-scale so that an inverse cascade of energy can develop concurrently with the direct cascade of energy. These are left for future work.

We finally note that it is argued in [75] that the anomalous diffusivity governing small-scale behavior and mixing is the same for active scalars such as temperature (or density) and for any passive scalar carried along by the fluid, since it is based on a vertical displacement of Lagrangian particles which can nevertheless be diagnosed through an Eulerian analysis [76,77]. Thus, it will be of interest to pursue this large parametric study taking into account the dynamics of Lagrangian particles in rotating stratified turbulence.

Author contribution statement

All authors contributed equally to the paper.

Duane Rosenberg acknowledges support from the Oak Ridge Leadership Computing Facility at ORNL via the DOE Office of Science under Contract No. DE-AC05-00OR22725. Raffaele Marino was supported by the Regional Operative Program Calabria ESF 2007/2013 as well as the Marie Curie Project FP7PIRSES-2010-269297-Turbo-plasmas. Annick Pouquet is thankful to the Laboratory for Atmospheric and Space Physics, University of Colorado, and to Bob Ergun for support. The National Center for Atmospheric Research is sponsored by the National Science Foundation. Computer time was also provided by the GTP (Geophysical Turbulence Program) and the ASD (Accelerated Scientific Discovery) programs at NCAR.

References

1. T. Ishihara, T. Gotoh, Y. Kaneda, Annu. Rev. Fluid Mech. **41**, 165 (2009).
2. D. Porter, A. Pouquet, P. Woodward, Phys. Rev. E **66**, 026301 (2002).
3. P. Mininni, A. Pouquet, Phys. Rev. E **80**, 025401 (2009).
4. R. Marino, L. Sorriso-Valvo, V. Carbone, P. Veltri, A. Noullez, R. Bruno, Planetary Space Sci. **59**, 592 (2011).
5. R. Marino, L. Sorriso-Valvo, R. D'Amicis, V. Carbone, R. Bruno, P. Veltri, Astrophys. J. **750**, 41 (2012).
6. E. D'Asaro, C. Lee, L. Rainville, R. Harcourt, L. Thomas, Science **332**, 318 (2011).
7. T. Peacock, M. Mercier, H. Didelle, S. Viboud, T. Dauxois, Phys. Fluids **21**, 121702 (2009).
8. V.E. Zakharov, V.S. Lvov, G. Falkovich, *Non-linear dynamics* (Springer, 1992).
9. P. Sagaut, C. Cambon, *Homogeneous Turbulence Dynamics* (Cambridge University Press, Cambridge, 2008).
10. A. Newell, V. Zakharov, Phys. Lett. A **372**, 4230 (2008).
11. S. Nazarenko, *Wave Turbulence*, Vol. **825** (Springer-Verlag, 2011).
12. K. Polzin, Y. Lvov, Rev. Geophys. **49**, RG4003 (2011).
13. V.E. Zakharov, A.O. Korotkevich, A. Pushkarev, D. Resio, Phys. Rev. Lett. **99**, 164501 (2007).
14. S. Lukaschuk, S. Nazarenko, S. McLelland, P. Denissenko, Phys. Rev. Lett. **103**, 044501 (2009).
15. A. Newell, B. Rumpf, Annu. Rev. Fluid Mech. **59**, 59 (2011).
16. G. Kolmakov, P. Vaughan, P.E. McClintock, S. Nazarenko, Proc. Nat. Acad. Sci. U.S.A. **111**, 4727 (2014).
17. S. Galtier, Phys. Rev. E **68**, 015301 (2003).
18. S. Galtier, J. Plasma Phys. **72**, 721 (2006).
19. J. Sun, C.J. Nappo, L. Mahrt, D. Belusic, J.J. Finnigan, C. Yagüe, B. Grisogono, A. Pouquet, D.R. Stauer, R.B. Smith *et al.*, Rev. Geophys. **53**, 1 (2015) doi:10.1002/2015RG000487.
20. Y. Zhou, Phys. Fluids **7**, 2092 (1995).
21. S. Galtier, A. Pouquet, A. Mangeney, Phys. Plasmas **12**, 092310 (2005).
22. S. Nazarenko, S. Schekochihin, J. Fluid Mech. **677**, 134 (2011).
23. P.R. Imazio, P. Mininni, Phys. Scr. **T155**, 014037 (2013).
24. T. Teitelbaum, P. Mininni, Phys. Rev. Lett. **103**, 014501 (2009).
25. T. McDougall, R.J. Greatbatch, Y. Lu, J. Phys. Oceanogr. **32**, 1574 (2002).
26. P. Mininni, D. Rosenberg, R. Reddy, A. Pouquet, Parallel Comput. **37**, 316 (2011).
27. S. Chen, D.D. Holm, L.G. Margolin, R. Zhang, Physica D Nonlinear Phenom. **133**, 66 (1999).
28. J. Baerenzung, P. Mininni, A. Pouquet, D. Rosenberg, J. Atmos. Sci. **68**, 2757 (2011).
29. J. Graham, D. Holm, P.D. Mininni, A. Pouquet, J. Sci. Comput. **41**, 21 (2011).
30. S. Venayagamoorthy, D. Stretch, J. Fluid Mech. **564**, 197 (2006).
31. E. Deusebio, G. Boffetta, E. Lindborg, S. Musacchio, Phys. Rev. E **90**, 023005 (2014).
32. D. Luketina, J. Imberger, J. Geophys. Res. **94**, 12619 (1989).
33. L. Liechtenstein, F. Godeferd, C. Cambon, J. Turb. **6**, 1 (2005).
34. L. Liechtenstein, F. Godeferd, C. Cambon, Flow Turb. Combust. **76**, 419 (2006).
35. R. Marino, P. Mininni, D. Rosenberg, A. Pouquet, Phys. Rev. E **90**, 023018 (2014).
36. H. Liu, V. Yudin, R. Roble, Geophys. Res. Lett. **40**, 665 (2013).

37. A. Newell, S. Nazarenko, L. Biven, Physica D **152-153**, 520 (2001).
38. Y.V. Lvov, S. Nazarenko, Phys. Rev. E **69**, 066608 (2004).
39. E. Falcon, S. Fauve, C. Laroche, Phys. Rev. Lett. **98**, 154501 (2007).
40. C. Rorai, P. Mininni, A. Pouquet, Phys. Rev. E **89**, 043002 (2014).
41. A. Naso, A. Pumir, M. Chertkov, J. Turb. **7**, N41 (2006).
42. J. Sun, L. Mahrt, R. Banta, Y. Pichugina, J. Atmos. Sci. **69**, 338 (2012).
43. H. Peters, M. Gregg, J. Toole, J. Geophys. Res. **93**, 1199 (1988).
44. A. Pumir, B.I. Shraiman, Phys. Rev. Lett. **75**, 3114 (1995).
45. P. Bartello, private communication (2015).
46. R. Marino, D. Rosenberg, C. Herbert, A. Pouquet, EPL **112**, 49001 (2015).
47. D. Stretch, S. Venayagamoorthy, Geophys. Res. Lett. **37**, L02602 (2010).
48. B. Sawford, J.F. Pinton, *A Lagrangian view of turbulent dispersion and mixing*, Vol. *Ten chapters in Turbulence*, edited by P.A. Davidson, Y. Kaneda, K.R. Sreenivasan (Cambridge University Press, 2013).
49. I. Mazzitelli, F. Fornarelli, A. Lanotte, P. Oresta, Phys. Fluids **26**, 055110 (2014).
50. J.P. Laval, J.C. McWilliams, B. Dubrulle, Phys. Rev. E **68**, 036308 (2003).
51. W. Smyth, J. Moum, J. Phys. Oceanogr. **31**, 1969 (2001).
52. G. Ivey, K. Winters, J. Koseff, Annu. Rev. Fluid Mech. **40**, 169 (2008).
53. P. Bartello, J. Atmos. Sci. **52**, 4410 (1995).
54. P. Billant, J.M. Chomaz, Phys. Fluids **13**, 1645 (2001).
55. E. Lindborg, J. Fluid Mech. **550**, 207 (2006).
56. A. Renaud, A. Venaille, F. Bouchet, ArXiv1505:01356 (2015).
57. A. Sozza, G. Boffetta, P. Muratore-Ginanneschi, S. Musacchio, Phys. Fluids **27**, 035112 (2015).
58. E. Lindborg, G. Brethouwer, J. Fluid Mech. **614**, 303 (2008).
59. D. Stretch, J. Rottman, S. Venayagamoorthy, K. Nomura, C.R. Rehmann, Dyn. Atmos. Oceans **49**, 25 (2010).
60. M. Waite, C. Snyder, J. Atmos. Sci. **66**, 883 (2009).
61. G. Bordes, F. Moisy, T. Dauxois, P. Cortet, Phys. Fluids **24**, 014105 (2012).
62. E. Lindborg, Geophys. Res. Lett. **32**, 1 (2005).
63. M. Waite, P. Bartello, J. Fluid Mech. **568**, 89 (2006).
64. R. Marino, A. Pouquet, D. Rosenberg, Phys. Rev. Lett. **114**, 114504 (2015).
65. A.M. Brunner-Suzuki, M. Sundermeyer, M.P. Lelong, J. Phys. Oceanogr. **44**, 2446 (2014).
66. L.M. Smith, F. Waleffe, J. Fluid Mech. **451**, 145 (2002).
67. R. Marino, P. Mininni, D. Rosenberg, A. Pouquet, EPL **102**, 44006 (2013).
68. C. Herbert, R. Marino, A. Pouquet, D. Rosenberg, submitted to J. Fluid Mech. (2015), arXiv.org/1509.02549.
69. A. Rahimi, A. Chandy, J. Turb. **17**, 1 (2015).
70. C. Rorai, D. Rosenberg, A. Pouquet, P. Mininni, Phys. Rev. E **87**, 063007 (2013).
71. R. Hide, Geophys. Astrophys. Fluid Dyn. **7**, 157 (1976).
72. R. Marino, P. Mininni, D. Rosenberg, A. Pouquet, Phys. Rev. E **87**, 033016 (2013).
73. A. Pouquet, D. Rosenberg, R. Marino, C. Herbert, submitted to J. Fluid Mech. (2015).
74. F. Baer, J. Tribbia, Month. Weather Rev. **105**, 1536 (1977).
75. E. Lindborg, E. Fedina, Geophys. Res. Lett. **36**, L01605 (2009).
76. R. Sturman, S. Wiggins, New J. Phys. **11**, 075031 (2009).
77. K. McIlhany, S. Guth, S. Wiggins, Phys. Fluids **27**, 063603 (2015).